ARTICLE   **OPEN**

Check for updates

Surface interfacial analysis of simulant high level nuclear waste glass dissolved in synthetic cement solutions

Claire L. Corkill [1 ✉], Colleen Mann[1], Jeremy R. Eskelsen[2], Donovan N. Leonard[2], Lucy M. Mottram[1], Martin C. Stennett [1], Jennifer M. S. Ayling[1], Clare L. Thorpe [1], Max R. Cole[1], Sarah Nicholas [3], Ryan Tappero[3] and Eric M. Pierce [2]

The corrosion mechanisms and kinetics of a Mg-rich alkali aluminoborosilicate glass simulating UK high-level waste (CaZn28) were investigated upon dissolution in synthetic cement solutions. Dissolution varied as a function the different pH and alkali/alkaline earth content of each cement solution. High resolution microscopy and spectroscopy techniques ascertained the nature of the interface between the glass and the cement solutions. TEM-EDS revealed alkali- and alkaline earth-rich silica gels, into which K, Ca and Mg were incorporated. TEM-SAED, combined with synchrotron micro-focus XRD, identified the ubiquitous precipitation of the Mg-aluminate layered double hydroxide phase, meixnerite ($Mg_6Al_2(OH)_{18}\cdot4H_2O$), in addition to goethite (FeOOH) and crystalline silica. The C-S-H phase, tobermorite ($Ca_5Si_6O_{16}(OH)_2\cdot4H_2O$), was identified in the most Ca-rich solution only. These data give insight to the role of alkali/alkaline earth-rich solutions in the dissolution or radioactive waste glasses, of importance to the final disposition in a geological disposal facility.

INTRODUCTION

Reprocessing of spent nuclear fuel produces highly radioactive fission product-containing residues that are immobilised in an alkali aluminoborosilicate glass. This material, known as vitrified high-level waste (HLW), is considered to be passively stable for the amount of time it will take for the radioactivity of the fission products to decay to "safe" levels, on the order of 100,000 years. During this time, the HLW will be isolated within a geological disposal facility (GDF), some hundreds of metres below the ground. Once here, it is expected that it will eventually come into contact with groundwater, partially dissolve and form alteration products.

In a GDF, cement materials will be ubiquitous, being used as seals, plugs and lining for disposal vaults and in general construction. The Supercontainer concept for HLW disposal in Belgium uses Portland Cement to encase the vitrified waste[1,2], while other countries with large inventories of cementitious waste (e.g., the UK) aim to separate vitrified waste from cementitious materials due to the possible negative consequences caused by high pH groundwater solution contacting HLW glass[3]. On the one hand, hyperalkaline conditions will increase the solubility of silica, enhancing glass dissolution rates, but on the other, high concentrations of alkali (Na, K) and alkaline earth (predominantly Ca) elements, generated during the dissolution of cement minerals by groundwater, may lower the dissolution rate of the glass by becoming incorporated in passivating silica gel layers[4–11]. While there have been many studies of HLW glass corrosion at near-neutral and high pH, there are far fewer that investigate the dissolution in simulant or realistic cement solutions[12–16]. A number of questions remain; for example, it is yet to be fully ascertained how silica gel layer formation is influenced by cement solutions, and research evaluating the extent to which cement solutions contribute to the so-called "rate resumption" stage of glass dissolution is at early stages[12,17,18].

The role of Ca^{2+} in glass dissolution at high pH, being present in both the dissolution media (e.g. $Ca(OH)_2$) and within the glass itself, is relatively well understood[5–8,10,19–21]. However, other divalent cations likely to influence glass dissolution have not been as thoroughly investigated, especially under hyperalkaline conditions. In the UK, vitrified HLW contains high concentrations (4–6 wt.%) of Mg from the reprocessing of Magnox fuel, which used Mg-Al alloy fuel cladding. Under near-neutral conditions, the presence of Mg^{2+} in HLW glass has been shown to significantly enhance the corrosion rate[22,23] due to the preferential formation of Mg-silicate minerals upon dissolution, which lowers the saturation of silica in solution, thus providing a thermodynamic driver for further glass dissolution[23–28]. But at higher pH values, of >pH 10, where the solubility of Mg-silicates and Mg-hydroxides is different, the influence on dissolution rates is poorly understood. The UK HLW glass formulation has been recently modified to contain a small proportion of Ca and Zn[21,29–32], and it has been shown that Zn^{2+} may play a similar role to Mg^{2+} in accelerating glass leaching[24,32–36]; this behaviour at high pH has yet to be determined.

The current study aims to investigate the influence of synthetic cement solutions on the dissolution of the UK HLW glass, CaZn28, using an inactive surrogate. The solutions utilised represent three different stages of cement mineral dissolution by groundwater[37], with compositions ranging from high alkali content at pH 13.5 (Young Cement Water)[11,13,14], to high alkaline-earth content at pH 12.5 (Evolved Cement Water)[11], and a composition much lower in both alkali and alkali-earth elements at pH 11.7 (Old Cement Water)[11]. Using an accelerated dissolution methodology, we aim to elucidate the mechanisms and kinetics of dissolution in each of these solutions, to understand the role of cement water chemistry on silica gel layer formation, and to evaluate the role of secondary phase formation on the dissolution process.

---

[1]Immobilisation Science Laboratory, Department of Materials Science and Engineering, University of Sheffield, Sheffield, UK. [2]Oak Ridge National Laboratory, Oak Ridge, TN, USA. [3]Brookhaven National Laboratory, NSLS-II, Upton, NY, USA. ✉email: c.corkill@sheffield.ac.uk

RESULTS

The influence of cement water type on dissolution kinetics

The Young Cement Water (YCW) solution was initially rich in K ($\sim$9000 mg L^{-1}) and Na ($\sim$2900 mg L^{-1}). When in contact with crushed glass powders (at an initial geometric surface area to solution volume ratio of 1200 m^{-1}), the average pH was close to that of the blank YCW solution, at pH(RT) 13.50 $\pm$ 0.43 (compared with 13.54 $\pm$ 0.03 in the blank, Supplementary Material Fig. 1). Showing two regimes of dissolution over 120 days, the normalised residual dissolution rate (NR$_B$), based on a linear fit to the boron normalised mass loss (NL$_B$) data shown in Fig. 1a, was an order of magnitude higher for YCW than for glass dissolved in the other solutions, and more than double that of the same glass dissolved in pure water[33] (Table 1). This is in agreement with previous observations of glass dissolution in YCW solution, which found that the formation of a porous K-rich alkali silica gel enhanced the diffusion of ions between the glass and solution relative to the lower porosity gel layer formed in initially pure water[13].

Initially (between 1 and 21 d), the glass dissolution in YCW was rapid and characterised by an accelerated increase in the concentration of all elements. This behaviour is broadly consistent with the definition of the "initial" dissolution rate, where ion exchange and silica hydrolysis control the dissolution behaviour[38]. This period of dissolution was defined as NR$_{B,initial}$ (Fig. 1a, Table 1). After this time, all of the elements showed a change in behaviour consistent with the onset of the residual rate, where dissolution is controlled by silica saturation, the formation of transport-limiting silica gel and secondary silicate phases, and subsequent diffusion of elements through the gel layer[38,39]. During this period, termed NR$_{B,residual}$, the NL$_{Zn}$ and NL$_{Al}$ decreased, which was concurrent with a plateau in NL$_{Si}$, suggestive of the formation of secondary Zn,Al-containing secondary silicate phases or gel layers. Interestingly, the NL$_{Mg}$ increased with experimental duration, which is contrary to previous studies of UK HLW glass (MW25) dissolved in near-neutral solutions, where Mg-silicate secondary phase precipitation is associated with a decrease in NL$_{Mg}$[17–20]. The concentration of K in solution was reduced by 12% during NR$_{B,initial}$, when compared to that of the blank solution, and by a further 31% during NR$_{B,residual}$ (see Supplementary Material Fig. 2), indicating that a K-rich alkali-silica gel or K-bearing secondary phases were formed.

The Evolved Cement Water (ECW), containing no K, but relatively high concentrations of Ca (290 mg L^{-1}) and Na (210 mg L^{-1}) had an average pH(RT) of 12.30 $\pm$ 0.50, similar to the blank value of pH 12.46 $\pm$ 0.01 (Supplementary Material Fig. 1). The dissolution rate was significantly lower than that obtained for YCW (NR$_{B,residual}$, Table 1) and approximately 4 times lower than that obtained for the same glass dissolved in initially pure water (Table 1). This is in agreement with a wide range of studies that show the presence of Ca in the leaching medium reduces the dissolution rate of glass, at least in the short term, by the formation of a passivating dense Ca-silica gel[5–8,10]. Indeed, there was an appreciable reduction in the Ca concentration when compared to the blank solution: 86% of the Ca originally added was removed from solution by 112 d (Table 1), implicating this element in the formation of Ca-rich silica alteration layers.

Unlike glass dissolved in YCW, only one regime of dissolution was observed for CaZn28 dissolved in ECW: there was a sustained (linear) increase in NL$_B$, NL$_{Li}$, NL$_{Al}$ and NL$_{Mg}$, which is typically indicative of the "initial" rate of dissolution. The release of Si and Zn, however, was zero (or below detection limits) for the duration of the experiment, suggestive of Si-Zn gel layer or secondary phase formation, which is typically associated with the "residual" rate of dissolution. This behaviour has also been referred to as a "lag" or "induction" period[5–8], where the NL$_B$ is yet to plateau despite the apparent formation of a gel layer/secondary phases. It points towards sustained dissolution/re-precipitation of silica-bearing phases that drive dissolution of the glass network at a rapid rate.

The Old Cement Water (OCW) contained a lower concentration of Na (65 mg L^{-1}), a significantly lower concentration of Ca ($\sim$4 mg L^{-1}) compared to the ECW solution, and no K. The pH throughout the course of the experiment was pH(RT) 11.40 $\pm$ 0.85 on average, which was the same as that of the blank solution, within error (pH(RT) 11.71 $\pm$ 0.02). The rate of dissolution was similar to that derived for glass dissolved in ECW solution, albeit somewhat lower, and all of the Ca in solution was slowly removed over the course of $\sim$70 d (Table 1). Analysis of the NL behaviour showed a similar trend to the glass dissolved in ECW solution, with a linearly increasing NL$_B$ and NL$_{Li}$ throughout the duration of the experiment. However, in contrast to the ECW solution, it was possible to detect Si. The NL$_{Si}$ was low, and showed some minor fluctuation, but it generally increased throughout the duration of the experiment. Due to the proximity of solution concentrations to the detection limits, it is difficult to draw conclusions about the behaviour of NL$_{Mg}$ and NL$_{Al}$. It was not possible to detect Zn, implying that it was retained in the glass alteration products.

Surface analysis of glass reacted in Young Cement Water

To verify the nature of the alteration layers formed during dissolution in YCW, glass grains allowed to react for 84 d were analysed in detail. Focussed Ion Beam (FIB) sections were taken from glass grains embedded in epoxy resin and analysed by Scanning Transmission Electron Microscopy (STEM), as shown in Fig. 2. An amorphous silica gel layer, $\sim$1.7 µm thick, was found to form a sharp interface with the pristine glass dissolved in YCW (Fig. 2a). EDS analysis of the gel layer revealed it to be rich in K and Al compared to the pristine glass, consistent with the formation of a K-rich alkali silica gel (Table 2)[13]. The gel layer was also somewhat enriched in Fe, Mg and Zr, and depleted in Na, when compared with the bulk glass composition. Analysis of the TEM image by pore diameter determination (PDD) gave an approximate gel porosity of 1.3 nm (Fig. 3), which was more than double that observed in gel layers formed by ECW and OCW solutions. It should be noted that while damage to the gel layers by the electron beam was not observed, such an effect cannot be precluded.

On top of the K-rich alkali-silica gel, a layer of precipitates, $\sim$0.5 µm thick, was observed. These loosely packed silicate-ribbons were highly enriched in Mg (with a content of $\sim$10 at.% greater than the bulk glass, Table 2), K, Fe and contained appreciable Al (Table 2). The morphology and elemental constituents of these phases are consistent with the formation of clay minerals, such as the trioctahedral magnesium smectites (saponite, hectorite) observed upon the dissolution of Mg-rich glass by several authors[23–28].

It was not possible to identify the mineral phase by bulk XRD (Supplementary Material Fig. 3) and there was a lack of positive confirmation from SAED analysis (Fig. 2e), likely due to electron beam damage to the sample, especially given that clay phases are hydrous and susceptible to beam damage. As such, synchrotron µ-XRD analysis was performed by taking multiple diffraction patterns across the precipitate layer using an x-ray beam $\sim$2 µm^2 in size. Figure 4a–c show the corresponding µ-XRF chemical maps highlighting the Ca, Fe and Zn distribution, respectively, to aid depiction of the alteration layer; these are in good agreement with the TEM-EDS observations. Notably, there appears to be a "hot-spot" of Fe and a slight enrichment of Fe on the outer edge of the alteration layer (Fig. 4b). The µ-XRD patterns were summed (Fig. 4d) and the background subtracted (Fig. 4e) to reveal peaks that were indexed as FeOOH (PDF #01-074-3080) and the Mg-bearing phase, meixnerite (Mg$_6$Al$_2$(OH)$_{18}$·4H$_2$O; PDF #00-035-0965), both consistent with the high Fe and Mg content observed by TEM-EDS (Table 2). Meixnerite is a Mg-Al hydrotalcite group
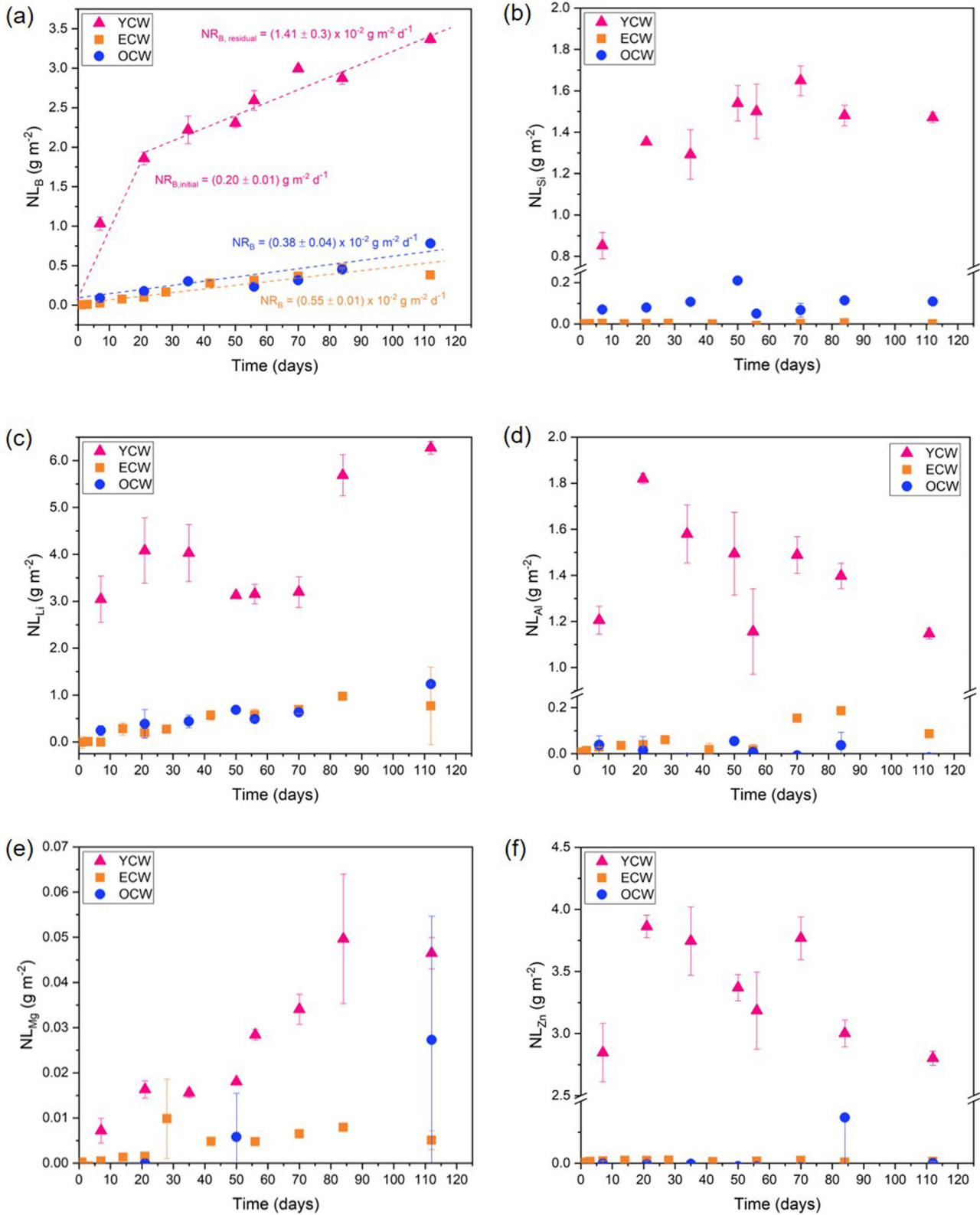
Fig. 1 Normalised mass loss (NL) of elements for CaZn28 glass dissolved in synthetic cement waters (YCW, ECW and OCW) at 50 °C for 112 d, at a glass surface area to solution volume ratio of 1200 m^{-1}. a NL$_B$, highlighting linear fit of the dissolution rates (NR$_B$); **b** NL$_{Si}$; **c** NL$_{Li}$; **d** NL$_{Al}$; **e** NL$_{Mg}$ and; **f** NL$_{Zn}$. Errors represent one standard deviation of triplicate measurements.

Table 1. Measured solution parameters for CaZn28 glass dissolved in synthetic cement solutions.

Solution	Average pH(RT)	B dissolution rate (NR$_B$, g m^{-2} d^{-1})[a]	R^2	Δ$_K$ (%)[b]	Δ$_{Ca}$ (%)[b]	RF$_{Al}$ (%)[c]	RF$_{Si}$ (%)[c]
Young Cement Water							
NR$_{B, initial}$ (1–21 d)	13.50 ± 0.43	0.20 ± 0.01	0.92	−12%	-	2	27
NR$_{B, residual}$ (21–112 d)		(1.41 ± 0.30) × 10^{-2}	0.89	−31%	-	66	56
Evolved Cement Water							
NR$_B$ (1–112 d)	12.30 ± 0.50	(0.55 ± 0.01) × 10^{-2}	0.99	-	−86%	77	99
Old Cement Water							
NR$_B$ (1–112 d)	11.40 ± 0.85	(0.38 ± 0.04) × 10^{-2}	0.97	-	−100%	100	91
UHQ[33]							
NR$_{B, initial}$ (1–35 d)	9.30 ± 0.20	(2.00 ± 0.50) × 10^{-2}	0.97	-	-	56	80

Errors stated are the standard deviation of triplicate measurements.
[a]Calculated by linear regression over the time period stated.
[b]The change in K and Ca concentrations when compared with the blank solution.
[c]Retention factors (RF) for Al and Si, in %, with an error of ±1%.

mineral with a double layered hydroxide structure. As it cannot easily take K into its structure, the high K (and Si) content observed in the precipitate region by TEM-EDS (Table 2) suggests that meixnerite may nucleate within the K-rich alkali silica gel. However, it is also possible that the EDS beam measured both gel layer and precipitates within the same point analysis, accounting for the K content. Also identified by μ-XRD was RuO$_2$, which is present in the unaltered glass (Supplementary Material Fig. 3) and hydrated crystalline silica (SiO$_2$·nH$_2$O; PDF #00-038-0448).

Neither FeOOH nor meixnerite were predicted to form by geochemical modelling of the solution data, although it should be noted that thermodynamic data for the latter phase is not currently available and utilisation of the thermodynamic database at high pH is somewhat limited. The K-rich zeolite phase, phillipsite-K (K$_6$Al$_6$Si$_{10}$O$_{32}$·12H$_2$O), previously observed to form during the dissolution of glasses in the presence of YCW solution[13,40], was predicted to be saturated in solution after 70 d, and several Mg- and K-bearing silicates were found to be saturated including: brucite [Mg(OH)$_2$], saponite [(Ca$_{0.25}$(Mg,Fe)$_3$((Si,Al)$_4$O$_{10}$)(OH)$_2$·n(H$_2$O)], and vermiculite-K [K$_{1.4}$(Mg,Fe,Al)$_6$(Si,Al)$_8$O$_{20}$(OH)$_4$·8H$_2$O]. The Zn-silicate metamorphic mineral, willemite (Zn$_2$SiO$_4$), was also predicted to be saturated in solution and, although this phase is unlikely to form, it may point towards the propensity of the solution to precipitate other hydrous Zn-silicates not available in the thermodynamic database employed[33,36].

Surface analysis of glass reacted in Evolved Cement Water

Examination of the glass altered for 84 d in ECW solution, by STEM-EDS, revealed a gel layer with a total thickness of ~0.5 μm, with an average (mode) pore diameter of approximately 0.5 nm (Fig. 3). The layer had a Ca content that was ~17 at.% greater than the pristine glass, and also exhibited high Fe, Zr and Zn concentrations (Table 2). The Si and Al concentrations were somewhat lower than in the pristine glass, and there was significantly less Na and Mg (Table 2). Needle precipitates were observed to grow throughout the gel layer (Fig. 5), extending outwards and adhering individual glass particles together (Fig. 5a). This is significant, since such behaviour may reduce the reactive surface area exposed to solution and thus, when normalised to the surface area, the reported dissolution rate could be underestimated.

Bright and dark field STEM images showed two distinct types of precipitate: fibrous needle-like precipitates and a dense precipitate. Both were significantly enriched in Ca (>50 at.% more Ca than in the pristine glass) and contained Al and Si, with the needle precipitate containing twice as much Si as the dense precipitate (Table 2). Mg was present in the dense precipitate only, but in a concentration lower than that of the pristine glass (Table 2). The two types of precipitate were further differentiated by diffraction analysis; SAED patterns for the dense precipitate showed some crystallinity, but it was not possible to index the pattern given the extent of diffuse scattering (Fig. 5e). The SAED pattern for the needle precipitate returned a diffraction pattern that could be partially indexed as the C-S-H mineral, tobermorite (Ca$_5$Si$_6$O$_{16}$(OH)$_2$·4H$_2$O) (Fig. 5d, Supplementary Material Fig. 4), consistent with the geochemical modelling prediction that this phase was saturated in solution for the duration of the experiment. Such was the extent of precipitation of C-S-H, that tobermorite was also indexed in the bulk XRD analysis (Supplementary Material Fig. 3), in addition to calcite (CaCO$_3$) and portlandite (Ca(OH$_2$)).

Micro-focus x-ray analysis was performed on monolith samples exposed to ECW for 84 d (Fig. 6). These particular samples were first washed in de-ionised water (a strong solvent) to remove the outer-tobermorite precipitate, thus enabling determination of mineral phases present within (rather than without) the gel layer. Ca was enriched in the outer ~2.5 μm of the glass sample (Fig. 6a), and a Zn-bearing region (albeit at a lower concentration than present in the glass) was observed on the outer-most surface (Fig. 6c). Fe was evenly distributed in the pristine glass and gel layer, suggesting the Fe leached from the glass was retained. The summed and background subtracted μ-XRD patterns taken throughout the upper 2.5 μm of the sample surface presented Bragg reflections that could be indexed as meixnerite, FeOOH and hydrated crystalline silica (as for the YCW solution) (Fig. 6e).

Surface analysis of glass reacted in Old Cement Water

The FIB-STEM analysis for glass exposed to OCW solution for 84 d is shown in Fig. 7. An amorphous silica gel layer, ~1 μm thick, was observed, that was enriched in Si, Al, K, Ca Fe and Zr relative to the pristine glass. It was depleted in Na, Mg and Zn (Table 2). The average gel porosity was the same as that observed for glass dissolved in ECW, with an approximate value of 0.5 nm (Fig. 3). A layer of ribbon-like precipitates, ~2 μm thick and similar in morphology to smectite clays observed by Curti et al.[22], resided on top of the gel layer (Fig. 7b). These had an elevated Mg-content (more than double the at.% in the pristine glass), also contained Na, Al, Ca, K, Zn and Si (Table 2). Identification of the ribbons was not possible, since the SAED patterns revealed an amorphous structure (Fig. 7e); moreover, it was not possible to identify any crystalline phases by
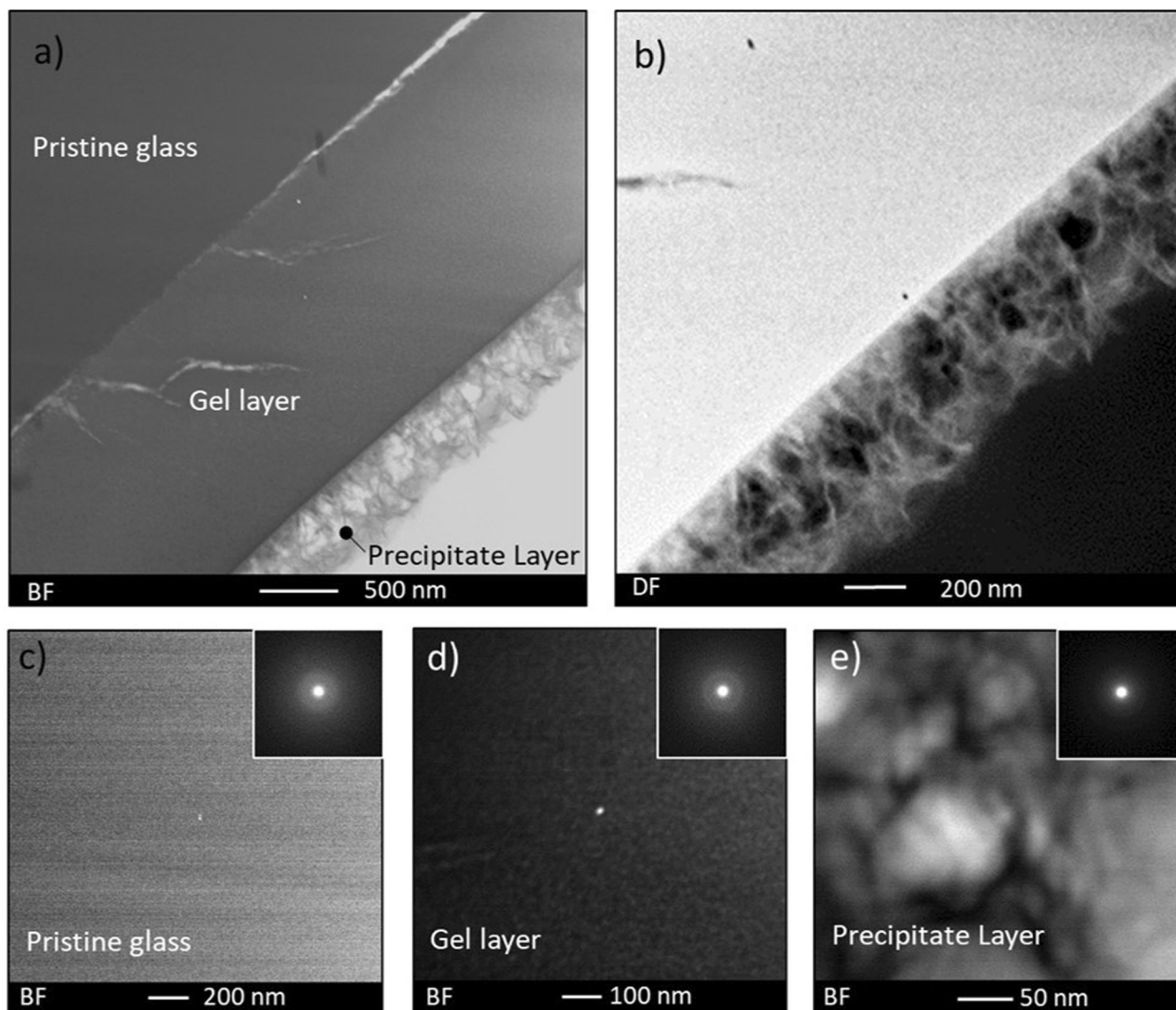
Fig. 2 Scanning transmission electron microscopy analysis of CaZn28 glass after 84 d of dissolution in Young Cement Water. a Image showing the cross section of the pristine glass, gel layer and precipitate layer; (**b**) dark field micrograph of the gel layer and Mg-silicate rich ribbon precipitates; and high resolution bright field images and associated selective area electron diffraction patterns of: (**c**) the pristine glass; (**d**) the gel layer; and (**e**) the precipitates.

μ-XRD analysis (data not shown). This implies that either no crystalline phases were present or that they were smaller than the x-ray beam size (~2 μm^2) and thus lacked sufficient intensity for identification.

Given the lack of phase identification, geochemical modelling of the solution chemistry was performed to indicate which phases may be thermodynamically favourable to precipitate from solution. A wide range of phases – containing M^{2+} (Ca or Mg), Al and Si – were found to be saturated in solution, including: hydrotalcite ($Mg_6Al_2CO_3(OH)_{16}\cdot4(H_2O)$), which is the carbonate counterpart of meixnerite; the Mg-bearing phyllosilicate clays saponite ($Ca_{0.25}(Mg,Fe)_3((Si,Al)_4O_{10})(OH)_2\cdot n(H_2O)$) and montmorillonite [$(Na,Ca)_{0.3}(Al,Mg)_2Si_4O_{10}(OH)_2\cdot n(H_2O)$]; tobermorite ($Ca_5Si_6O_{16}(OH)_2\cdot4H_2O$); and the Ca-zeolites scolecite ($CaAl_2Si_3O_{10}\cdot3H_2O$) and zeolite CaP ($Ca_2Al_4Si_4O_{16}\cdot9H_2O$). FeOOH was also predicted, which may explain the dense outer layer observed in the precipitate region (Fig. 7a, b). Only calcite was detected by bulk XRD analysis (Supplementary Material Fig. 3). The alteration layer was smaller than the resolution afforded by SEM (Supplementary Material Fig. 5), in accordance with the low dissolution rates obtained.

DISCUSSION

It is evident from these results that the composition and pH of the synthetic cement solution had a quantifiable influence on the dissolution kinetics of CaZn28 glass, while also strongly influencing the nature of alteration layers formed. While it is challenging to unravel the effects of pH distinctly from those of solution composition using the data obtained in the present study, using the spatially resolved chemical and diffraction analysis of the alteration layer afforded by STEM and synchrotron μ-XRD techniques, it is possible to draw a range of conclusions regarding glass dissolution behaviour in these cement solutions.

In the highest pH solution, YCW, the dissolution rate of B was greatest. Moreover, the mean gel layer porosity, estimated by TEM analysis, was more than 2 times greater for the YCW solution than the ECW and OCW solutions. This behaviour, attributed to electrostatic repulsion of dissolved Si species at the surface of the glass, hinders the Ostwald ripening of Si-OH in the gel layer. This has previously been linked to enhanced diffusion of species, such as B, through the gel layer[13], explaining the enhanced dissolution rates observed in this solution.

Table 2. Elemental composition (at.%) for the alteration layers of CaZn28 dissolved in synthetic cement solutions, acquired by STEM-EDS.

	STEM-EDS composition (at.% ± 1%)									
	Si	Al	K	Na	Ca	Mg	Fe	Zr	Zn	Ln[a]
Pristine glass	25.7	1.9	0.1	6.8	6.4	5.7	0.1	0.3	2.4	1.4
YCW										
Gel layer	22.3	2.2	9.0	2.7	6.3	6.5	1.3	0.9	2.3	2.6
Precipitates	17.3	1.7	11.5	4.4	1.9	15.4	2.7	0.2	1.3	0.4
ECW										
Gel layer	21.7	1.0	0.0	0.9	23.4	0.9	1.5	1.1	1.3	6.9
Dense precipitate	6.5	0.5	0.1	0.0	52.3	2.9	0.5	0.4	1.3	2.3
Needle precipitate	13.7	0.5	0.1	0.4	45.3	0.1	0.7	1.0	1.5	0.0
OCW										
Gel layer	27.8	2.3	1.2	1.8	9.4	2.8	1.1	1.2	1.8	2.7
Precipitates	25.4	1.8	0.8	4.7	2.4	12.5	1.4	0.3	1.8	1.2

Spot analysis was conducted in the same locations as SAED. Stated error is the derived instrument quantification error.
[a]Ln represents lanthanide elements: Gd, La, Ce, Pr, Nd and Sm.

Contrasting dissolution behaviour was observed in the YCW and ECW/OCW solutions. In the former, the dissolution rate followed the "classic" regimes widely accepted to occur during alkali borosilicate glass dissolution. This included an initial increase in the NL_B, followed by a reduction in the dissolution rate associated with gel layer formation and precipitation of secondary phases. However, in the ECW and OCW solutions, glass dissolution did not follow the "classic" regimes. Instead, the normalised leaching of the soluble elements, B and Li, increased linearly, despite the low or negligible release of other elements including Si and Zn and the observation of gel layers. Such behaviour indicates that dissolution proceeded in the residual rate for the duration of the experiment, but the sustained, linear increase in NL_B and NL_{Li} suggests that the gel layers observed to form were not passivating. This seems unlikely given the smaller average pore diameter (~0.5 nm) when compared to that of the passivating YCW gel layer (~1.3 nm); therefore, an alternative explanation is required.

It is possible that the dissolution of the glass network in OCW and ECW solutions was accelerated by a dissolution/re-precipitation mechanism involving silicate[22,41–43] phases. Similar trends in the NL_i were recently reported to occur in CaZn28 glass dissolved in groundwater[33,34], which the authors attributed to the formation of the Zn-silicate clay, sauconite ($Na_{0.3}Zn_3(SiAl)O_{10}\cdot4H_2O$), and in the dissolution of MW25 (the CaZn-free counterpart of CaZn28), where it was attributed to the precipitation of Mg-silicate phases[5,22,44]. In the ECW solutions, C-S-H (tobermorite) was the only observed silicate precipitate, thus, it is likely that this mineral phase induced enhanced dissolution of the glass network. Without identification of the precipitated phase formed in the OCW solution it is not possible to assert which phase was responsible for this behaviour. There was no strong evidence that crystalline Zn-silicate phases influenced the dissolution behaviour.

It is also possible that a dissolution/re-precipitation mechanism involving the Mg-aluminate phase, mexinerite, could have the capacity to influence the overall glass dissolution reaction. We postulate that it is unlikely to drive continued dissolution in the same manner as Mg-silicates, if Al does not play a network forming role. If, on the other hand, if Al does participate directly in network formation, or if the Al utilised to form meixnerite is

obtained by dissolution of the silica gel layer (often rich in Al), then the formation of this phase may destabilise the gel, promoting further dissolution[26]. Since the NL_{Al} for all solutions continuously increased throughout the course of the experiments, this seems a less likely explanation for the observed behaviour than the dissolution/re-precipitation of silicate phases.

Comparison of the composition of the gel layer formed in each of the solutions was performed by normalisation of the STEM-EDS derived at.% values to Zr. Among the elements present in the glass (and easily detectable by EDS), Zr is the least soluble in the highly alkaline range and is, therefore, almost entirely retained in the glass alteration products (100% for ECW and OCW solutions, Supplementary Material Table 1). Caution must be taken when using this method for the YCW solution, since $HZrO_3^-$ tends to be soluble at pH values of > ~pH(RT) 12.6; however, since the Zr retention factor was consistently >99 ± 1% (Supplementary Material Table 1), this approach was deemed reasonable. Table 3 describes the average element/Zr ratios for the pristine glass, the gel layer and the precipitates for each of the cementitious solutions. Since it was not possible to detect Li by EDS, there are no data for this element; however, Li is considered in the following discussion for completeness.

The normalised atomic ratios highlight the strong influence of the alkali/alkaline-earth element content of each cement solution on the composition of the gel layer. For example, the K/Zr ratios in the gel layer of glass dissolved in YCW were much higher than in the pristine glass as a result of the incorporation of a significant amount of K from the solution. The Ca/Zr ratio of the gel layer formed in the ECW was significantly higher than that in the YCW and OCW solutions, which contained far less Ca. This confirms that the high uptake of Ca during the dissolution of glass ECW (Table 1) is related, at least in part, to incorporation within a silica gel. For the OCW solution, the gel layer was enriched in Al, K and Fe when compared with the pristine glass. Despite a high Na concentration in each of the solutions ($2900 ± 850$ mg L^{-1}, $212 ± 12$ mg L^{-1} and $65 ± 14$ mg L^{-1} in YCW, ECW and OCW, respectively), Na was not strongly retained in any of the gel layers. These observations indicate that although a mixture of alkali/alkaline-earth elements may be present within a solution (and, in the case of Mg, within the glass), some elements have a stronger affinity for incorporation in the gel layer than others, which is ultimately driven by the requirement to balance the negative charge of the silica gel layer at high pH values[45].

Making the assumption that Zr retention was the same in each of the solutions, it is possible to identify those alkali/alkaline-earth elements that are preferentially used in this charge balancing role. For the gel layer formed in YCW solution, the K/Zr ratio was the highest of all the alkaline and alkaline-earth elements, followed by Mg/Zr, Ca/Zr and Na/Zr (Table 3), giving a preferential order for gel layer incorporation of: $K^+ > Mg^{2+} \approx Ca^{2+} > Na^+$. For the ECW solution, the only element that was incorporated in the gel layer was Ca^{2+}, with a minor amount of Mg^{2+} and Na^+ (i.e., $Ca^{2+} > Mg^{2+} \approx Na^+$), while that formed in the OCW solution showed preferential incorporation of: $Ca^{2+} > Mg^{2+} > Na^+ > K^+$. Since the dominant secondary precipitate in all of the solutions was Mg-bearing meixnerite, caution should be taken with respect to interpreting the presence of Mg^{2+} in the EDS analysis of the gel, which may arise from over-sampling of the gel region by the electron beam.

Recent studies have considered the selectivity of hydrated silica surfaces for charge-compensating cations (Ca, K, Li, Na and Cs) in near-neutral pH solutions, and their role in passivating the dissolution of the International Simple Glass[9,10]. Based on several key thermodynamic and geochemical principles[9,46,47], an order of selective incorporation of alkali/alkaline-earth elements was postulated. According to the solvation sphere and hydration characteristics of each cation, the rate of dissociation of hydrated alkali and alkali-earth cations – otherwise known as the frequency
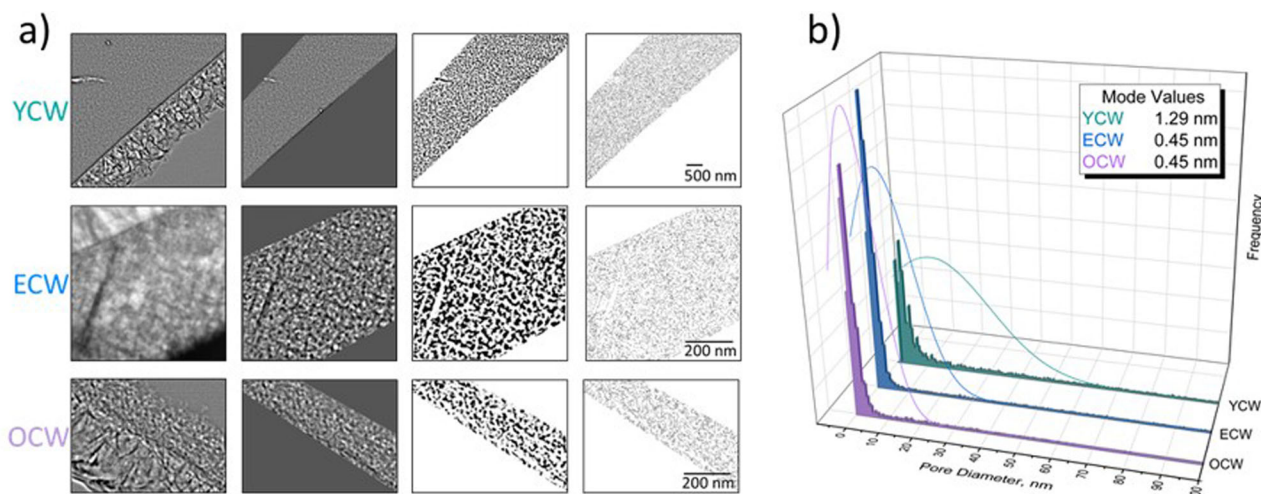
Fig. 3 Gel layer porosity data acquired from transmission electron microscopy images of CaZn28 exposed to synthetic cement solutions. Showing (**a**) the imaging processing steps required to acquire average pore diameter measurements (PDD), where pores are in white; and (**b**) the resulting histogram of the data obtained, listing the mode values.

of hydrated ion exchange, k_{ex} – occurs in the order: $K^+ > Na^+ > Li^+ > Ca^{2+} > Mg^{2+}$. Therefore, according to this principle, K is more likely to be incorporated within the silica gel layer than Na, Li, Ca or Mg. Such behaviour partially describes the observations in the YCW and ECW solutions, but not the OCW solution, where the K/Zr ratio was the lowest of all alkali / alkaline earth element to Zr ratios.

For the alkaline-earth cations an additional mechanism related to solvent properties may influence the propensity for incorporation in the gel layer. When divalent cations (M^{2+}) interact with silica surfaces, a proton is displaced, leaving the divalent cation partially hydrated, and positively charged at the surface (Eq. 1)[45,48]. The same process occurs for alkali elements (M^+), but without the positive charge (Eq. 2)[46]:

$$>SiO^- + M^{2+} \rightarrow >SiO - M^+ \qquad (1)$$

$$>SiO^- + M^+ \rightarrow >SiO - M \qquad (2)$$

As such, alkaline earth cations should exhibit stronger adsorption to the silica gel than alkali cations. It is also understood that sorption strength increases with increasing atomic radius within the group of the periodic table[46], albeit weakly in the case of the alkali cations, such that the adsorption coefficient (k_{ads}) for the elements of interest to the current study occurs in the order: $Ca^{2+} > Mg^{2+} > K^+ \approx Na^+ > Li^+$. This behaviour seems to be reflected in the composition of the gel layers formed in the ECW and OCW solutions, where Ca was incorporated preferentially over Mg, K and Na.

The nature of the secondary precipitates formed, or predicted to form, at the surface of the glass was also influenced by the synthetic cement water composition, and there were notable differences in the EDS elemental analysis of the precipitates formed in each solution. For example, precipitates in the ECW solution were enriched in Ca (Table 2), in accordance with microscopic and diffraction identification of the Ca-silicate mineral, tobermorite. The precipitates formed on the glass surface in the YCW solution were determined by EDS to contain K, and geochemical modelling predicted the saturation of phillipsite-K ($K_6Al_6Si_{10}O_{32}\cdot12H_2O$) in solution, although no K-bearing crystalline phase was identified experimentally. As noted previously, this may be due to oversampling of the precipitate region by the EDS beam (measuring K in the gel rather than precipitates), or the selection of an area with no K-bearing crystalline precipitates in the μ-XRD analysis. Notably, the precipitates formed on glass surfaces

exposed to YCW and OCW solutions were highly enriched in Mg in comparison to the pristine glass (Table 2). Together with the high Al/Zr ratios of the precipitates formed in these solutions (Table 3), this is in agreement with the experimental observation of the Mg-aluminate phase, meixnerite.

Meixnerite ($Mg_6Al_2(OH)_{18}\cdot4H_2O$)[49], shown in Fig. 8, is a high-surface area layered double-hydroxide mineral used in industrial applications such as catalysis[50], alcohol cyanoethylation in drug manufacture[51] and, through ion exchange of the interlayer OH^- ions, fluorine decontamination[52]. It is the hydroxide end-member of the Mg-carbonate cement phase, hydrotalcite ($Mg_2Al_6(OH)_{16}CO_3\cdot4H_2O$), which is known to readily accommodate a range of trivalent transition metals (Fe, Cr, Ni, Mn) within its structure e.g.[53], as well as having the capability to sorb divalent elements, such as Zn^{2+}, to its surface[54]. This may explain the slightly elevated concentrations of Zn associated with the precipitated phases formed in all cement solutions, especially the OCW.

The propensity of the CO_3-end member, hydrotalcite, to sorb actinides was recently explored[55], and it was determined that U^{6+} was sorbed to the surface in a Mg-carbonate type environment. Synthetic meixnerite, in solutions with a pH > 7.8, has been shown to incorporate MoO_4^{2-} ions[56], which may have advantages for radioactive waste glasses developed to immobilise high Mo waste-streams. Its capacity to sorb other anionic fission product radionuclides, e.g. SeO_4^{2-} or IO_3^-, does not seem to have been investigated in the wider literature.

Previous studies of the dissolution of UK HLW glass under near-neutral conditions have exclusively identified the presence of Mg-silicate precipitates such as sepiolite ($Mg_4Si_6O_{15}(OH)_2\cdot6H_2O$) and saponite ($Ca_{0.3}Mg_3(Si,Al)_4O_{10}(OH)_2\cdot4H_2O$) rather than Mg-aluminate phases[5,22]. The present study differs from those previously published in that high pH cement solutions were utilised. Under the conditions of glass dissolution in initially pure water, where the pH buffers to a value of ~9, Al exists as species such as $Al(H_2O)_4(OH)_2^+{}_{(aq)}$ and $Al(OH)_{3(aq)}$, in varying proportions, and tends to be preferentially utilised in charge compensation of the silica gel layer, or the formation of aluminosilicate-type phases such as zeolites or clay minerals[17,32,57–61]. At high pH, however, alumina is sparingly soluble, forming $Al(OH)_4^-{}_{(aq)}$ anions, which can be readily incorporated into the meixnerite structure as $[Al^{3+}(OH)_6]^{3-}$ species. This is exemplified by the NL_{Al} values (Fig. 1d), which show that, under all of the conditions investigated in the present study, Al was detected in solution for the duration
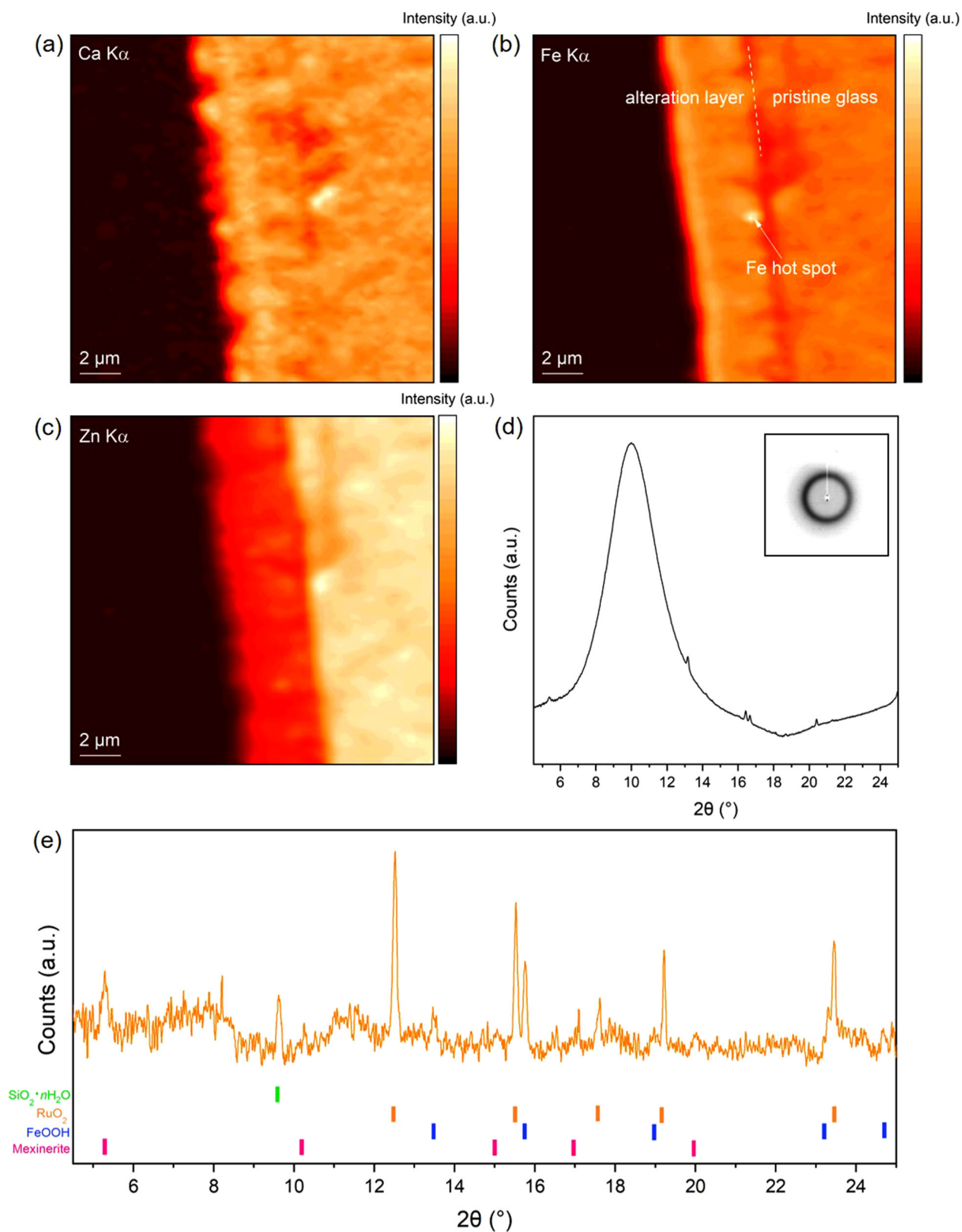
Fig. 4 Micro x-ray analysis of CaZn28 glass after 84 d of dissolution in Young Cement Water. Images showing the μ-XRF maps relating to the distribution of (**a**) Ca; (**b**) Fe; and (**c**) Zn. μ-XRD data are shown in (**d**) which depicts summed, un-calibrated, μ-XRD patterns with a 2D XRD pattern inset; and (**e**) showing the background subtracted, summed μ-XRD data. Phases were indexed as $SiO_2 \cdot nH_2O$ (PDF #00-038-0448); FeOOH (PDF #01-074-3080), meixnerite ($Mg_6Al_2(OH)_{18} \cdot 4H_2O$; PDF #00-035-0965) and RuO_2 (PDF #01-075-4303).
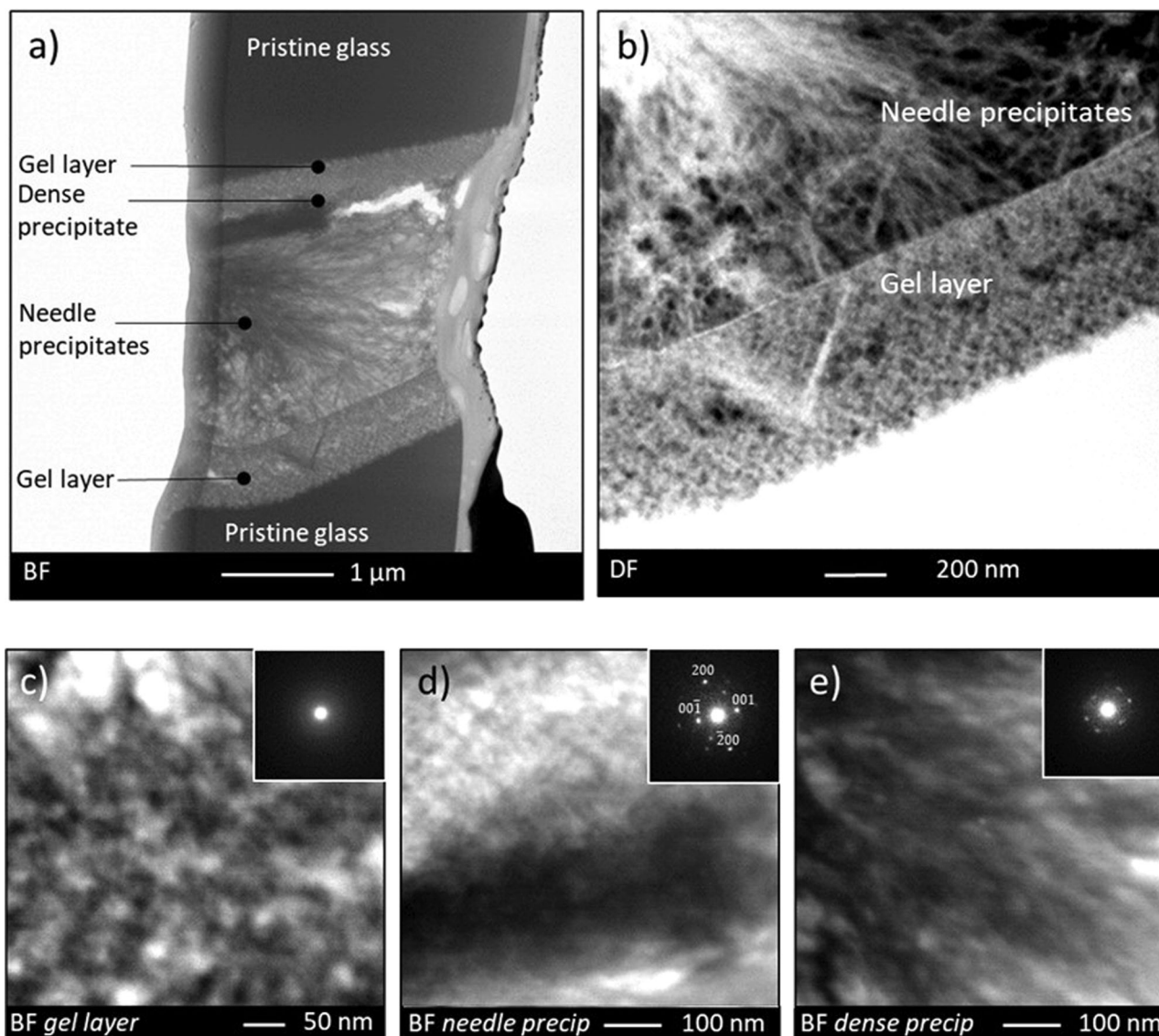
Fig. 5 Scanning transmission electron microscopy analysis of CaZn28 glass after 84 d of dissolution in Evolved Cement Water. a Bright field image showing the interface between two adjacent grains that had been cemented together by secondary phases, highlighting several regions of different morphology or chemistry; (**b**) dark field micrograph of the gel layer and Ca-silicate rich precipitates; and high resolution bright field images and associated selective area electron diffraction patterns of: (**c**) the gel layer; (**d**) the needle precipitates; and (**e**) the dense precipitate.

of the experiment. Synthetic meixnerite is commonly prepared *via* reaction of $Mg(OH)_2$ with $Al(OH)_4^-$ in alkaline solution, although usually under hydrothermal conditions (>200 °C)[55]. Since $Al(OH)_4^-$ tends to participate in condensation reactions more readily than silica anions, particularly at high pH, this may account for the ubiquitous presence of Mg-aluminate precipitates, rather than Mg-silicate precipitates, in the present study.

The precipitation of Al-bearing silicate zeolites is known to be an important factor in initiating Stage III (rate resumption) dissolution behaviour[59–62], however it is yet to be understood whether the precipitation of a Mg-Al phase, which does not contain silica, could result in the same behaviour. Clearly, after 112 d, there was no evidence of such behaviour in the present study. It is possible that depletion of Al, through the formation of aluminate phases, may eventually result in a more stable silicate gel layer. Further study of the role of this phase in high pH glass dissolution may be beneficial.

METHODS

Glass specimen preparation

The composition of the simulant UK nuclear waste glass, known as CaZn28, utilised in this study, is given in Table 4. This material differs somewhat from that used in historic UK HLW studies in that it is the Ca/Zn-modified version of MW25, now utilised on one of the three vitrification plants at Sellafield[32–36]. The designation "28" refers to the waste loading of 28 wt.%. CaZn28 was prepared using glass frit obtained from the Vitrification Test Rig at the National Nuclear Laboratory (batch number H0023/1 Ca/Zn ½ Li) and 28 wt.% simulant waste calcine (WRW17, which contained Ru and Li, from the National Nuclear Laboratory), with thanks to Dr. Mike Harrison. The calcine and frit were mixed prior to melting at 1050 °C in an alumina crucible for 4 h, poured into a pre-heated stainless steel mould, and the resulting glass ingot was annealed at 500 °C with a cooling rate of 0.5 °C min^{-1} until room temperature was attained. The glass was first sliced to obtain monoliths, with the remainder crushed to a powder for dissolution experiments. The density of the glass was measured by helium pycnometry (Micromeritics Accupyc II) to be 2.76 ± 0.14 g cm^{-3}.
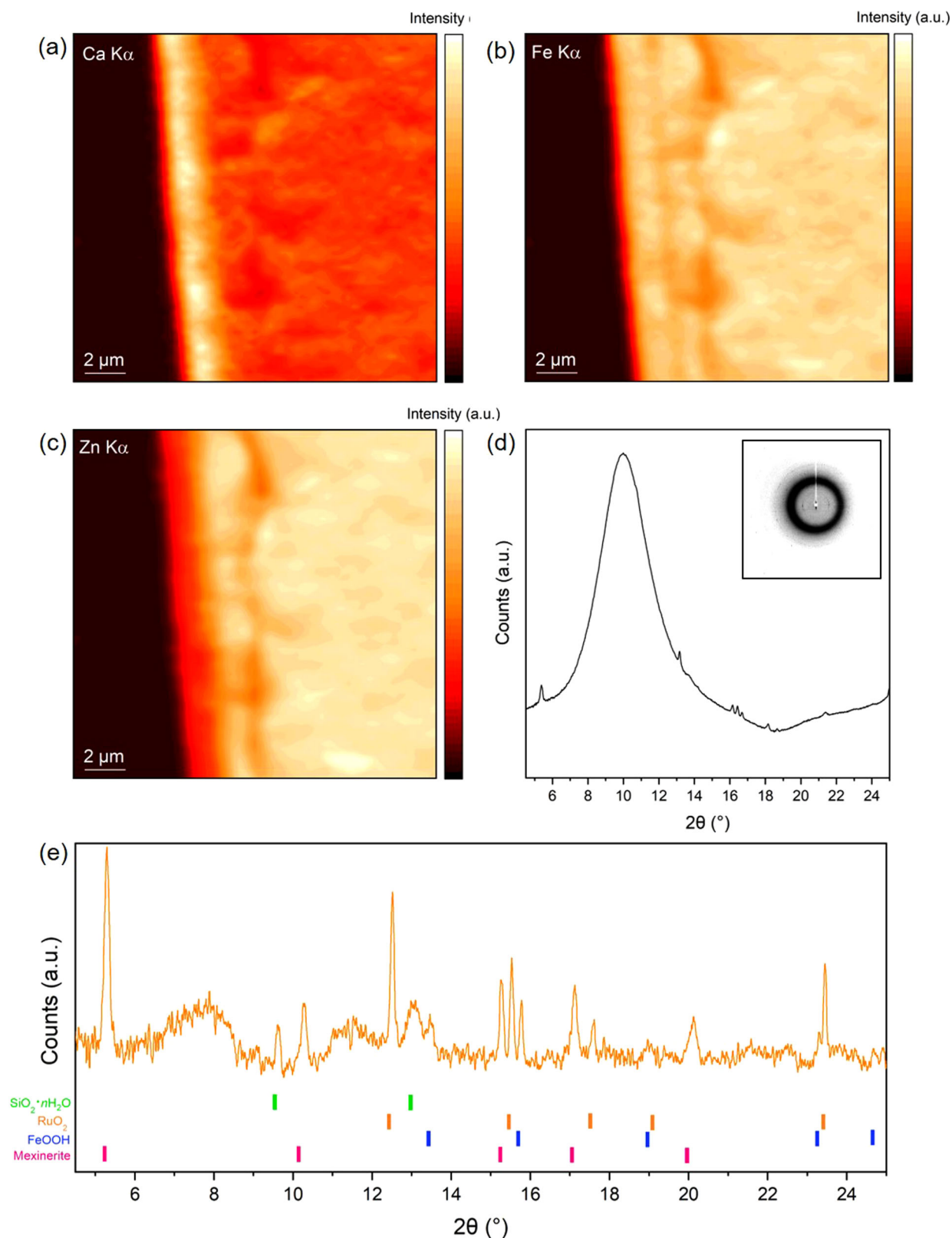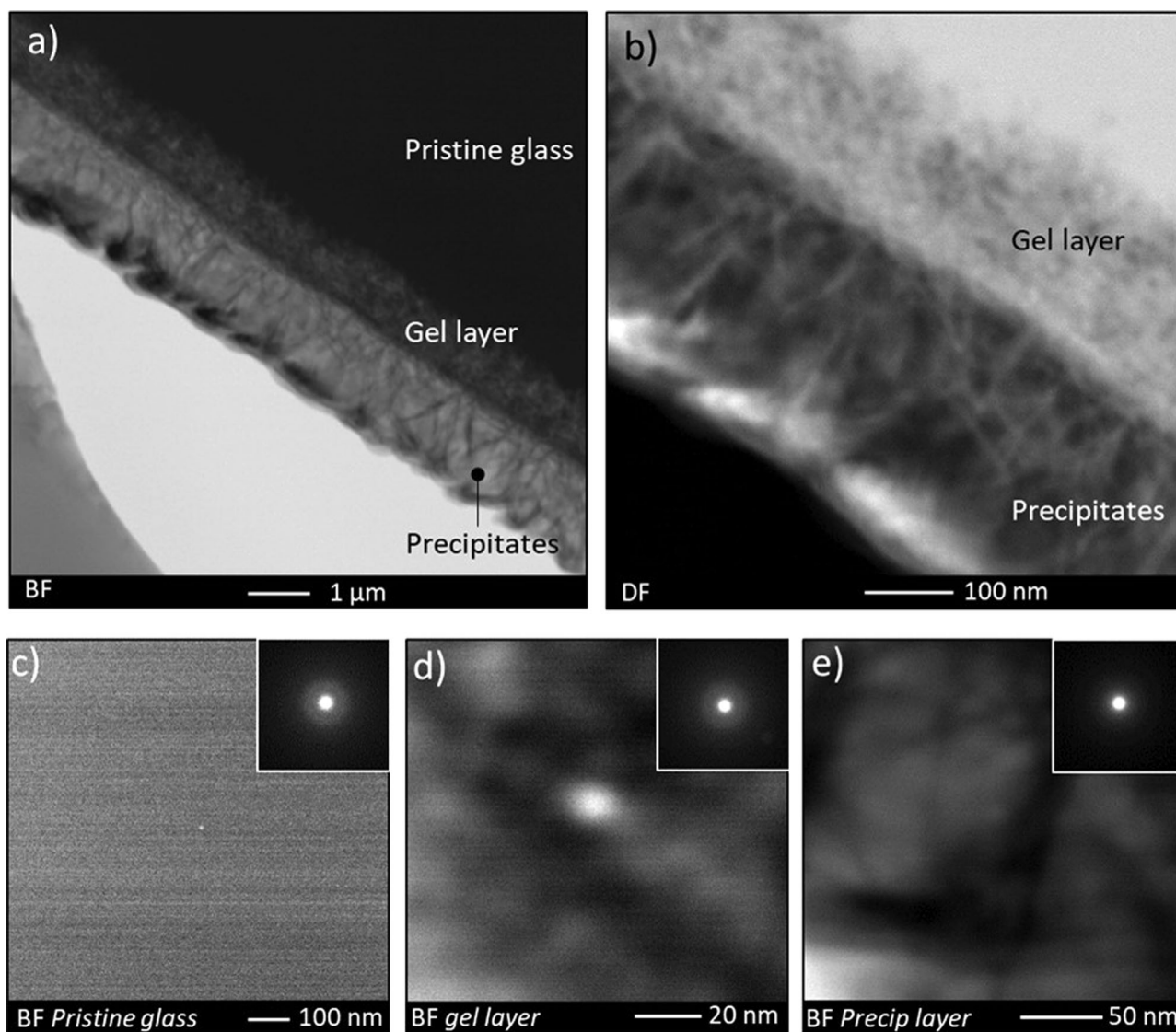
Fig. 6   Micro x-ray analysis of CaZn28 glass after 84 d of dissolution in Evolved Cement Water. Images showing the μ-XRF maps relating to the distribution of (**a**) Ca; (**b**) Fe; and (**c**) Zn. μ-XRD data are shown in (**d**) which depicts summed, un-calibrated, μ-XRD patterns with a 2D XRD pattern inset; and (**e**) showing the background subtracted, summed μ-XRD data. Phases were indexed as FeOOH (PDF #01-074-3080), meixnerite ($Mg_6Al_2(OH)_{18}\cdot4H_2O$; PDF #00-035-0965) and $SiO_2\cdot nH_2O$ (PDF #00-038-0448).

Fig. 7 Scanning transmission electron microscopy analysis of CaZn28 glass after 84 d of dissolution in Old Cement Water. a Bright field image showing the cross section of the pristine glass, gel layer and precipitate layer; (**b**) dark field micrograph of the gel layer sandwiched between the pristine glass and ribbon-like precipitates; and high resolution bright field images and associated selective area electron diffraction patterns of: (**c**) the pristine glass; (**d**) the gel layer; and (**e**) the precipitates.

Table 3. Average Zr-normalised atomic ratios of major elements in the pristine glass, the gel layer and the secondary precipitates, as determined by STEM-EDS.

	Pristine glass	Gel			Precipitate		
		YCW	ECW	OCW	YCW	ECW[a]	OCW
Si/Zr	86.82	25.10	19.53	25.05	78.08	14.23	85.71
Al/Zr	0.80	2.42	0.89	2.10	7.70	0.54	6.13
Mg/Zr	19.35	7.26	0.81	2.50	69.51	0.13	42.15
Ca/Zr	21.48	7.08	21.05	8.50	8.69	47.08	7.96
K/Zr	0.28	10.09	0.00	1.12	51.58	0.09	2.80
Na/Zr	22.80	3.01	0.80	1.60	19.71	0.46	15.78
Fe/Zr	0.47	1.42	1.39	1.01	11.97	0.73	4.72
Zn/Zr	8.14	2.62	1.16	1.59	5.79	1.59	5.97

[a]Needle precipitate.

Synthetic cement water preparation

The solutions utilised were based upon those developed by SCKCEN to represent the evolution of Portland cement pore water chemistry over geological time scales, involving the dissolution of cement minerals by clay groundwater[11,63]. Reagents utilised were: NaOH; KOH; Na_2SO_4; $Ca(OH)_2$; and $CaCO_3$ (all > 99% purity). Reagents were added to N_2-degassed ultra-high quality (UHQ) water (18 MΩ cm) within a Coy anaerobic chamber (O_2 and CO_2 < 1 ppm) purged with a $H_{2(g)}$ (5%)/$N_{2(g)}$ mix and left to equilibrate for 3 months. The three resulting compositions: Young Cement Water (YCW); Evolved Cement Water (ECW); and Old Cement Water (OCW), are shown in Table 5. It should be noted that there are some deviations in the elemental compositions of the cement solutions when compared with the SCKCEN cement solutions[11,63]; however, the relative proportions of elements and the final room temperature pH are similar.

Dissolution experiment methodology

Two types of dissolution experiment were performed: ASTM C1285-21 (PCT-B)[64] which uses powdered glass to accelerate dissolution progress, and ASTM C1220-17 (MCC-1)[65], which uses monolith samples to allow examination of surface alteration layers by microscopy. In the former, glass
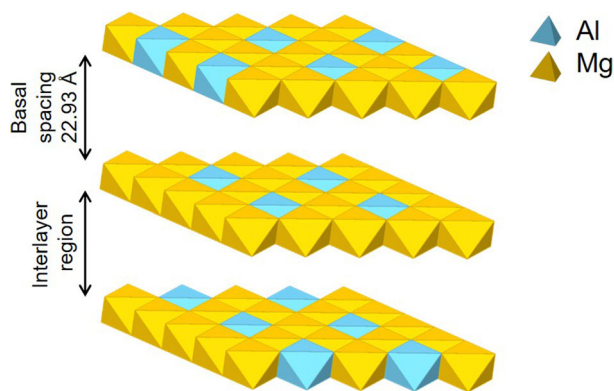
Fig. 8 Crystal structure of meixnerite ($Mg_6Al_2(OH)_{18}\cdot4H_2O$). Highlighting the layered double hydroxide structure, comprised of sheets containing $[Mg^{2+}(OH)_6]^{4-}$ (yellow) and $[Al^{3+}(OH)_6]^{3-}$ (cyan) tetrahedra, and interlayer regions where water and a wide range of anionic species can exist.

Table 4. Glass composition as measured by acid (aqua regia and HF) digest and ICP-OES analysis.

Oxide component	mol.% (±5%)
SiO_2	43.08
B_2O_3	18.43
Na_2O	7.31
Li_2O	7.08
MgO	5.86
CaO	5.33
Al_2O_3	5.28
ZnO	3.42
Fe_2O_3	0.99
ZrO_2	0.55
MoO_3	0.41
RuO_2	0.36
NiO	0.36
Nd_2O_3	0.27
Cs_2O	0.21
CeO_2	0.20
Cr_2O_3	0.18
SrO	0.15
BaO	0.12
La_2O_3	0.11
SO_3	0.07
$Pr2O3$	0.05
Sm_2O_3	0.05
Y_2O_3	0.04
Cu_2O	0.02
K_2O	0.01
TiO_2	0.01
Total	99.90

The error on all values is derived from the instrument analytical error, and is ±5%.

particles in the 75–150 µm size range were prepared and washed according to ASTM standard protocols, and placed in 15 mL PFA vessels. In the latter, polished (1 µm finish, diamond paste) glass coupons $10\times10\times1$ mm were placed in a PFA basket, within a 60 mL PFA vessel.

Synthetic cement solutions were added to the vessels containing glass inside the anaerobic chamber and the lids were tightened. The surface area to volume ratio (based on geometric calculation) was 1200 m^{-1} for powdered glass experiments and 400 m^{-1} for monoliths. The sealed vessels were then placed within a large air-tight container and transferred to an oven set at 50 ± 2 °C. The air-tight containers were constantly purged with $N_{2(g)}$ to prevent carbonation of the solutions by $CO_{2(g)}$ in the air.

Triplicate vessels containing glass, and duplicate blanks (no glass added), were sacrificed at 1, 3, 7, 14, 21, 28, 35, 50, 56, 70, 84, 112 days for the powdered experiments. At each time point, an aliquot was removed for pH measurement and the elemental concentrations were determined using Inductively Coupled Plasma-Optical Emission Spectroscopy (ICP-OES, ThermoScientific iCAP6300 Duo) utilising a ceramic torch and inert internal standard, after filtration (0.22 µm), acidification (ultrapure HNO_3) and dilution with UHQ water. From the concentration data, the normalised mass loss (NL_i, g m^{-2}) of element i, was calculated according to Eq. 3, where C_i is the concentration of element i (g m^{-3}); $C_{i,b}$ the concentration of i in the blank (g m^{-3}); f_i is the mass fraction of i in the glass; and SA/V is the geometric (spherical) glass surface area to volume ratio, in m^{-1}. The normalised dissolution rate (NR_i, g m^{-2} d^{-1}) of element i was calculated from a linear fit.

$$NL_i = \left(C_i - C_{i,b}\right)/\left(f_i \times \frac{SA}{V}\right) \tag{3}$$

The retention factor (RF_i) of element i (the percentage retained in the alteration product) was determined according to Eq. 4, after Curti et al.[22], where [E] is the molar concentration in solution of the element considered, [C] is the molar concentration of a congruently dissolving element (in the present study, B), f_E and f_C are the corresponding atomic elemental fractions in the unaltered glass, and NL_E, NL_C are the normalised mass losses.

$$RF_i = 100 \times \left(1 - \frac{[E]f_C}{[C]f_E}\right) = 100 \times \left(1 - \frac{NL_E}{NL_C}\right) \tag{4}$$

The pH of the solutions was measured at room temperature (~22 °C) inside the anaerobic chamber to prevent the solution from carbonating. The pH probe was calibrated at pH 10 and 12 prior to use and rinsed with UHQ water between samples. It should be noted that the pH measurements were not corrected for the high ionic strength of the leachates, therefore the values stated are indicative and not absolute.

Geochemical modelling was performed using the software package, PHREEQC, utilising the LLNL thermodynamic database. Solution concentrations and at-temperature pH values were used as input to the model.

Post-dissolution characterisation of glass

After 84 d of dissolution, the glass powders and monoliths were selected for analysis. Phase identification was performed by X-ray Diffraction (XRD) using a Bruker D2 Phaser X-ray Diffractometer, using Kα (λ = 1.5418 Å) radiation generated from a Cu target at a working voltage of 30 kV and 10 mA. A Ni filter and a Lynx-Eye position sensitive detector were used. An angular range 10° < 2Θ < 70° with a 0.02° step size progressing at 0.17° min^{-1} were applied, with a total scan time of 180 min. The samples were rotated at frequency of 60 Hz. The alteration layers of the powder samples were prepared using a Hitachi NB5000 dual focused ion beam scanning electron microscope (FIB-SEM) and examined using a cold field emission Hitachi HF-3300 high-resolution transmission electron microscope with an accelerating voltage of 300 keV at Oak Ridge National Laboratory, which has the capability to generate simultaneous secondary electron and STEM images. EDS was performed using a Bruker XFlash silicon drift detector (SDD) attached to the HF3300 TEM/STEM/SEM for elemental mapping of the FIB section. This was utilised to determine the composition and structure of the altered layers, while selective area electron diffraction (SAED) was utilised to identify mineral phases.

Image J was used to measure the average pore diameter using TEM images obtained as described above. The TEM images were processed with a fast Fourier transform (FFT) bandpass filter to exclude features larger than 100 pixels and smaller than 3 pixels to achieve an even brightness and to reduce noise. Black and white inversion highlighted pores in white for size analysis against the image scale.

Synchrotron radiation µ-focus X-ray analyses were conducted at the 4BM (XFM) beamline at the National Synchrotron Light Source-II, Brookhaven National Laboratory, USA. Glass monoliths, removed at various time points corresponding to sampling points of the powdered experiments, were

Table 5. Composition of synthetic cement waters (mg L^{-1}), as determined by ICP-OES.

	pH(RT)	Ca	Na	K	Al	Si	Mg	S
YCW	13.50 ± 0.3	-	2911.0 ± 850.0	9002.0 ± 324.1	-	-	-	63.5 ± 12.1
ECW	12.3 ± 0.5	290.0 ± 37.0	212.0 ± 22.0	-	0.6 ± 0.4	4.4 ± 2.1	0.2 ± 0.1	4.3 ± 1.2
OCW	11.5 ± 0.3	3.7 ± 0.2	65.1 ± 14.3	-	0.2 ± 0.0	-	-	5.3 ± 1.4

Errors represent one standard deviation of triplicate measurements.

prepared as thin sections (30 μm thick) mounted on 250 μm thick Spectrosil® slides. Slides were oriented at 45° to the direction of X-ray propagation and raster scanned through the micro-focused X-ray beam (spot size of ~2 μm^2). X-ray fluorescence (μ-XRF) was measured using a Canberra SXD 7-element SDD with Quantum Detectors Xspress3 electronics, mounted at 90° to the incident x-ray beam direction. Two-dimensional micro X-ray diffraction (μ-XRD) measurements were acquired using Perkin Elmer 1621 XRD area detector positioned behind the sample and calibrated to a LaB$_6$ standard. Diffraction data were acquired at a monochromatic beam energy of 18 keV. μ-XRF data were manipulated using the Larch open software package[66], while Dioptas[67] was used to convert 2D diffraction patterns to 1D for peak indexing using the Sieve+ ICDD database.

DATA AVAILABILITY

The data that support these findings are available upon reasonable request to the authors.

REFERENCES

1. Bel, J. J. P., Wickham, S. M. & Gens, R. M. F. Development of the supercontainer design for deep geological disposal of high-level heat emitting radioactive waste in Belgium. *Mater. Res. Soc. Symp. Proc.* **932**, 23–32 (2006).
2. Van Geet, M. & Weetjens, E. *Strategic choices in the Belgian supercontainer design and its treatment in the safety case. NEA/OECD Report number NEA/RWM/R(2012)3/REV*, 1–6 (2012).
3. *Geological disposal: steps towards implementation*. Nuclear Decommissioning Authority Report. NDA/RWMD/013 (2010).
4. Gin, S. et al. The fate of silicon during glass corrosion under alkaline conditions: a mechanistic and kinetic study with the International Simple Glass. *Geochim. Cosmochim. Acta* **151**, 68–85 (2015).
5. Corkhill, C. L., Cassingham, N. J., Heath, P. G. & Hyatt, N. C. Dissolution of UK high-level waste glass under simulated hyperalkaline conditions of a co-located geological disposal facility. *Int. J. Appl. Glas. Sci.* **4**, 341–356 (2013).
6. Chave, T., Frugier, P., Gin, S. & Ayral, A. Glass-water interphase reactivity with calcium-rich solutions. *Geochim. Cosmochim. Acta* **75**, 4125–4139 (2011).
7. Utton, C. A. et al. Chemical durability of vitrified wasteforms: effects of pH and solution composition. *Miner. Mag.* **76**, 2919–2930 (2012).
8. Utton, C. A., Hand, R. J., Hyatt, N. C., Swanton, S. W. & Williams, S. J. Formation of alteration products during dissolution of vitrified ILW in a high-pH calcium-rich solution. *J. Nucl. Mater.* **442**, 33–45 (2013).
9. Collin, M., Fournier, M., Charpentier, T., Moskura, M. & Gin, S. Impact of alkali on the passivation of silicate glass. *npj Mater. Degrad.* **2**, 16 (2018).
10. Aréna, H., Rébiscoul, D., Garcès, E. & Godon, N. Comparative effect of alkaline elements and calcium on alteration of International Simple Glass. *npj Mater. Degrad.* **3**, 10 (2019).
11. Liu, S., Ferrand, K. & Lemmens, K. Transport- and surface reaction-controlled SON68 glass dissolution at 30 °C and 70 °C and pH = 13.7. *Appl. Geochem.* **61**, 302–311 (2015).
12. Ferrand, K., Liu, S. & Lemmens, K. The interaction between nuclear waste glass and ordinary Portland cement. *Int. J. Appl. Glas. Sci.* **4**, 328–340 (2013).
13. Mann, C. et al. Influence of young cement water on the corrosion of the International Simple Glass. *npj Mater. Degrad.* **3**, 5 (2019).
14. Mann, C., Eskelsen, J. R., Leonard, D. N., Pierce, E. & Corkhill, C. L. The dissolution of simulant vitrified intermediate level waste in young cement water. *MRS Adv.* **5**, 131–140 (2020).
15. Andriambololona, Z., Godon, N. & Vernaz, E. R7T7 glass alteration in the presence of mortar – effect of the cement grade. *Mater. Res. Soc. Symp. Conf. Proc.* **257**, 151–158 (1992).
16. Berner, U. R. Evolution of pore water chemistry during degradation of cement in a radioactive waste repository environment. *Proc. Waste Manag.* **12**, 201–219 (1992).
17. Ribet, S. & Gin, S. Role of neoformed phases on the mechanisms controlling the resumption of SON68 glass alteration in alkaline media. *J. Nucl. Mater.* **324**, 152–164 (2004).
18. Mercado-Depierre, S., Fournier, M., Gin, S. & Angeli, F. Influence of zeolite precipitation on borosilicate glass alteration under hyperalkaline conditions. *J. Nucl. Mater.* **491**, 67–82 (2017).
19. Mercado-Depierre, S., Angeli, F., Frizon, F. & Gin, S. Antagonist effects of calcium on borosilicate glass alteration. *J. Nucl. Mater.* **441**, 402–410 (2013).
20. Backhouse, D. J., Corkhill, C. L., Hyatt, N. C. & Hand, R. J. Investigation of the role of Mg and Ca in the structure and durability of aluminoborosilicate glass. *J. Non Cryst. Solids* **512**, 41–52 (2019).
21. Fisher, A. J. et al. Chemical structure and dissolution behaviour of CaO and ZnO containing alkali-borosilicate glass. *Mater. Adv.* **3**, 1747–1758 (2022).
22. Curti, E., Crovisier, J. L., Morvan, G. & Karpoff, A. M. Long-term corrosion of two nuclear waste reference glasses (MW and SON68): a kinetic and mineral alteration study. *Appl. Geochem.* **21**, 1152–1168 (2006).
23. Maeda, T., Ohmori, H., Mitsui, S. & Banba, T. Corrosion behaviour of simulated HLW glass in the presence of magnesium ion. *Int. J. Corr.* **796457**, 1–7 (2011).
24. Thien, B. J. et al. Structural identification of a tricoctahedral smectite formed by the aqueous alteration of a nuclear glass. *Appl. Clay Sci.* **49**, 135–141 (2010).
25. Thien, B. M. J., Godon, N., Ballestero, A., Gin, S. & Ayral, A. The dual effect of Mg on the long-term alteration rate of AVM nuclear waste glasses. *J. Nucl. Mater.* **427**, 297–310 (2012).
26. Aréna, H. et al. Impact of Zn, Mg, Ni and Co elements on glass alteration: additive effects. *J. Nucl. Mater.* **470**, 55–67 (2016).
27. Jollivet, P. et al. Effect of clayey groundwater on the dissolution rate of the simulated nuclear waste glass SON68. *J. Nucl. Mater.* **420**, 508–518 (2012).
28. Debure, M. et al. Mineralogy and thermodynamic properties of magnesium phyllosilicates formed during the alteration of a simplified nuclear glass. *J. Nucl. Mater.* **475**, 255–265 (2016).
29. Dunnett, B. F. *Summary of the development of a Ca/Zn borosilicate glass for vitrification of high molybdenum waste*. National Nuclear Laboratory Report: NNL(13)12642, Issue 1 (2013).
30. Harrison, M. T. & Brown, G. C. Chemical durability of UK vitrified high level waste in Si-saturated solutions. *Mater. Lett.* **221**, 154–156 (2018).
31. Dunnett, B. F. et al. Vitrification of high molybdenum waste. *Glass Tech.: Eur. J. Glass Sci. Tech.* **53**, 166–171 (2012).
32. Cassingham, N. J., Stennett, M. C., Bingham, P. A. & Hyatt, N. C. The structural role of Zn in nuclear waste glasses. *Int. J. Appl. Glass Sci.* **2**, 343–353 (2011).
33. Fisher, A. J. et al. Short communication: The dissolution of UK simulant vitrified high-level-waste in groundwater solutions. *J. Nucl. Mater.* **538**, 1–7 (2020).
34. Fisher, A. J. *Dissolution of UK vitrified high level radioactive waste containing zinc and calcium*. PhD Thesis, The University of Sheffield (2020).
35. Zhang, H. et al. Effect of Zn- and Ca-oxides on the stucture and chemical durability of simulant alkali borosilicate glasses for immobilisation of UK high level wastes. *J. Nucl. Mater.* **462**, 321–328 (2015).
36. Cassingham, N. J., Corkhill, C. L., Stennett, M. C., Hand, R. J. & Hyatt, N. C. Alteration layer formation of Ca- and Zn-oxide bearing alkali borosilicate glasses for immobilisation of UK high level waste: a vapour hydration study. *J. Nucl. Mater.* **479**, 639–646 (2016).
37. Berner, U. R. Evolution of pore water chemistry during degradation of cement in a radioactive waste repository environment. *Waste Manag.* **12**, 201–209 (1992).
38. Gin, S., Frugier, P., Jollivet, P. & Bruguier, F. New Insight into the residual rate of borosilicate glasses: Effect of S/V and glass composition. *Int. J. Appl. Glass Sci.* **4**, 371–382 (2013).
39. Gin, S. et al. Insights into the mechanisms controlling the residual corrosion rate of borosilicate glasses. *npj Mater. Degrad.* **4**, 41 (2020).

40. Mann, C., Le Hoh, T., Thorpe, C. L. & Corkhill, C. L. Dissolution of glass in cementitious solutions: an analogue study for vitrified waste disposal. *MRS Adv.* **3**, 1147–1154 (2018).

41. Geisler, T. et al. Aqueous corrosion of borosilicate glass under acidic conditions: a new corrosion mechanism. *J. Non-Cryst. Solids* **356**, 1458–1465 (2010).

42. Geisler, T. et al. The mechanism of borosilicate glass revisited. *Geochim. Cosmochim. Acta* **158**, 112–129 (2015).

43. Lenting, C. et al. Towards a unifying mechanistic model for silicate glass corrosion. *npj Mater. Degrad.* **2**, 28 (2018).

44. Backhouse, D. J. *A study of the dissolution of nuclear waste glasses in highly-alkaline conditions*. PhD Thesis, The University of Sheffield (2016).

45. Iler, R. K. *The Chemistry of Silica*. John Wiley & Sons, Inc., (1979).

46. Dove, P. M. & Nix, C. J. The influence of the alkaline earth cations, magnesium, calcium, and barium on the dissolution kinetics of quartz. *Geochim. Cosmochim. Acta* **61**, 3329–3340 (1997).

47. Icenhower, J. P. & Dove, P. M. The dissolution kinetics of amorphous silica into sodium chloride solutions: Effects of temperature and ionic strength. *Geochim. Cosmochim. Acta* **64**, 4193–4203 (2000).

48. Boehm, H. P. & Schneider, M. Über die Bindung von aluminium aus aluminium-chlorid-lösungen an siliciumdioxid-oberflächen. *Z. Anorg. Allg. Chem.* **316**, 128–133 (1962).

49. Koritnig, S. & Süsse, P. Meixnerit, $Mg_6Al_2(OH)_{18} \cdot 4H_2O$, ein neues magnesium-aluminium-hydroxid-mineral. *Tscher. Miner. Petrog.* **22**, 79–87 (1975).

50. Prinetto, F., Ghiotti, G., Durand, R. & Tichit, D. Investigation of acid-base properties of catalysts obtained from layered double hydroxides. *J. Phys. Chem. B.* **104**, 11117–11126 (2000).

51. Cuautli, C., Valente, J. S., Conesa, J. C., Ganduglia-Pirovano, M. V. & Ireta, J. Theoretical study of the catalytic performance of activated layered double hydroxides in the cyanoethylation of alcohols. *J. Phys. Chem. C.* **123**, 8777–8784 (2019).

52. Guo, Q. & Reardon, E. J. Fluoride removal from water by meixnerite and its calcination product. *Appl. Clay Sci.* **56**, 7–15 (2012).

53. Zhang, F., Du, N., Zhang, R. & Hou, W. Mechanochemical synthesis of Fe_3O_4@(Mg-Al-OH LDH) magnetic composite. *Powder Technol.* **228**, 250–253 (2012).

54. Bankauskaite, A. & Baltakys, K. The formation of different Mg-Al LDHs (Mg/Al = 2:1) under hydrothermal conditions and their application for Zn^{2+} ions removal. *Sci. Sinter.* **46**, 95–106 (2014).

55. Yorkshire, A. S. et al. Spectroscopic evidence of UVI-cement mineral interactions: ettringite and hydrotalcite. *J. Sync. Rad.* **29**, 89–102 (2022).

56. Putyera, K., Jagiello, J., Bandosz, T. J. & Schwarz, J. A. Surface chemical heterogeneity of pillared hydrotalcites. *J. Chem. Soc. Faraday Trans.* **92**, 1243–1247 (1996).

57. Swaddle, T. W. Silicate complexes of aluminium(III) in aqueous systems. *Coord. Chem. Rev.* **219–221**, 665–686 (2001).

58. Jantzen, C. M., Trivelpiece, C. L., Crawford, C. L., Pareizs, J. M. & Pickett, J. B. Accelerated Leach Testing of GLASS (ALTGLASS): I. Informatics approach to high level waste glass gel formation and aging. *Int. J. Appl. Glass Sci.* **8**, 69–83 (2017).

59. Jantzen, C. M., Brown, K. G. & Pickett, J. B. Durable glass for thousands of years. *Int. J. Appl. Glass Sci.* **1**, 38–62 (2010).

60. Crum, J. V. et al. Seeded stage III glass dissolution behavior of a statistically designed glass matrix. *J. Am. Ceram. Soc.* **104**, 4145–4162 (2021).

61. Neeway, J. J. et al. Acceleration of glass alteration rates induced by zeolite seeds at controlled pH. *Appl. Geochem.* **113**, 104515 (2020).

62. Fournier, M., Gin, S. & Frugier, P. Resumption of nuclear glass alteration: state of the art. *J. Nucl. Mater.* **448**, 348–363 (2014).

63. Wang, L. *Near-field chemistry of a HLW/SF repository in Boom Clay – scoping calculations relevant to the supercontainer design*. SCK.CEN report number ER_17 (2009).

64. ASTM International. *ASTM C1285-21: Standard Methods for Determining Chemical Durability of Nuclear, Hazardous and Mixed Waste Glasses and Multiphase Glass Ceramics: The Product Consistency Test (PCT)* (2021).

65. ASTM International. *ASTM C1220-17: Standard Test Method for Static Leaching of Monolithic Waste Forms for Disposal of Radioactive Waste* (2017).

66. Newville, M. Larch: an analysis package for XAFS and related spectroscopies. *J. Phys.: Conf. Ser.* **430**, 012007 (2013).

67. Prescher, C. & Prakapenka, V. B. DIOPTAS: a program for reduction of two-dimensional X-ray diffraction data and data exploration. *High. Press. Res.* **35**, 223–230 (2015).

68. Hyatt, N. C. et al. The HADES facility for high activity decommissioning and science: part of the UK National Nuclear User Facility. *IOP Conf. Ser.: Mater. Sci. Eng.* **818**, 012022 (2020).

AUTHOR CONTRIBUTIONS

C.C. – funding acquisition, conceptualisation, data collection, formal analysis, original draft preparation, supervision, reviewing and editing. C.M. – data collection, formal analysis, draft preparation. J.E. – data collection, formal analysis. D.L. – data collection, formal analysis. J.A. – formal analysis and reviewing. C.T. – formal analysis, reviewing and editing. L.M. – data collection, formal analysis and reviewing. M.S. – data collection, formal analysis and reviewing. S.N. – data collection, reviewing and editing. R.T. – data collection, reviewing and editing. E.P. – funding acquisition, supervision, formal analysis, data collection, reviewing and editing.

COMPETING INTERESTS

The authors declare no competing interests.

ADDITIONAL INFORMATION

Supplementary information The online version contains supplementary material available at https://doi.org/10.1038/s41529-022-00279-5.

Correspondence and requests for materials should be addressed to Claire L. Corkhill.

Reprints and permission information is available at http://www.nature.com/reprints

Publisher's note Springer Nature remains neutral with regard to jurisdictional claims in published maps and institutional affiliations.